International Journal of Numerical Methods for Heat & Fluid Flow

Electromagnetic field analysis and cooling system design for high power switched reluctance motor

Wei-Mon Yan, Hsu-Yang Teng, Chun-Han Li, Mohammad Ghalambaz,

Electromagnetic field analysis and cooling system design for high power switched reluctance motor

Wei-Mon Yan
Department of Energy and Refrigerating Air-Conditioning Engineering, National Taipei University of Technology, Taipei, Taiwan and Research Center of Energy Conservation for New Generation of Residential, Commercial, and Industrial Sectors, National Taipei University of Technology, Taipei, Taiwan

Hsu-Yang Teng
Department of Energy and Refrigerating Air-Conditioning Engineering, National Taipei University of Technology, Taipei, Taiwan

Chun-Han Li
Department of Energy and Refrigerating Air-Conditioning Engineering, National Taipei University of Technology, Taipei, Taiwan and Research Center of Energy Conservation for New Generation of Residential, Commercial, and Industrial Sectors, National Taipei University of Technology, Taipei, Taiwan, and

Mohammad Ghalambaz
Department of Mechanical Engineering, Dezful Branch, Islamic Azad University, Dezful, Iran

Abstract

Purpose – The electromagnetic field and cooling system of a high power switched reluctance motor (SRM) are studied numerically. The geometry of the motor and its main components are established using a computer-aided design software in the actual size. This study aims to evaluate the resulting thermal losses using the electromagnetic analysis of the motor.

Design/methodology/approach – In the electromagnetic analysis, the Joule's loss in the copper wires of the coil windings and the iron losses (the eddy currents loss and the hysteresis loss) are considered. The flow and heat transfer model for the thermal analysis of the motor including the conduction in solid parts and convection in the fluid part is introduced. The magnetic losses are imported into the thermal analysis model in the form of internal heat generation in motor components. Several cooling system approaches were introduced, such as natural convection cooling, natural convection cooling with various types of fins over the motor casing, forced conviction air-cooled cooling system using a mounted fan, casing surface with and without heat sinks, liquid-cooled cooling system using the water in a channel shell and a hybrid air-cooled and liquid-cooled cooling system.

The authors appreciate the financial support from Ministry of Science and Technology, Taiwan, under grant number MOST 106-2221-E-027-103. The authors also appreciate the financial support by the "Research Center of Energy Conservation for New Generation of Residential, Commercial, and Industrial Sectors" from The Featured Areas Research Center Program within the framework of the Higher Education Sprout Project by the Ministry of Education (MOE) in Taiwan.

International Journal of Numerical Methods for Heat & Fluid Flow

0961-5539
DOI 10.1108/HFF-08-2018-0450

Findings – The results of the electromagnetics analysis show that the low rotational speed of the motor induces higher currents in coil windings, which in turn, it causes higher copper losses in SRM coil windings. For higher rotational speed of SRM, the core loss is higher than the copper loss is in SRM due to the higher frequency. An air-cooled cooling system is used for cooling of SRM. The results reveal when the rotational speed is at 4,000 rpm, the coil loss would be at the maximum value. Therefore, the coil temperature is about 197.9°C, which is higher than the tolerated standard temperature insulation material. Hence, the air-cooled system cannot reduce the temperature to the safe temperature limitation of the motor and guarantee the safe operation of SRM. Thus, a hybrid system of both air-cooled and liquid-cooled cooling system with mounting fins at the outer surface of the casing is proposed. The hybrid system with the liquid flow of Re = 1,500 provides a cooling power capable of safe operation of the motor at 117.2°C, which is adequate for standard insulation material grade E.

Originality/value – The electromagnetic field and cooling system of a high power SRM in the presence of a mounted fan at the rear of the motor are analyzed. The thermal analysis is performed for both of the air-cooled and liquid-cooled cooling systems to meet the cooling demands of the motor for the first time.

Keywords Switched reluctance motor, Total enclosed fan-cooled design, Electromagnetic field analysis, Liquid cooling system

Paper type Research paper

Nomenclature

B = Magnetic flux density (wb/m^2);
C_2 = Turbulent constant;
C_μ = Turbulent constant;
C_p = specific heat (kJ/kg-K);
d = Steel sheet thickness (mm);
D = Hydraulic diameter (m);
e = Back EMF (V);
f = Commutation frequency (Hz);
F = The friction coefficient of the motor;
G_k = Turbulent flow energy production;
L_z = Length of motor in z direction (m);
h = Convective heat transfer coefficient (W/m^2K);
$\overline{h}$ = Average convection heat transfer coefficient (W/m^2K);
I = Current (A);
J = The rotational momentum of the motor;
k = Thermal conductivity (W/mK);
L = Phase inductance (H);
m = Reluctance motor excitation phase;
N = Motor revolutions per minute (rpm);
n = Normal vector to a surface;
p = Pressure (Pa);
P_{copper} = Copper loss (W);
P_e = Eddy current loss (W);
P_h = Magnetic hysteresis loss (W);
P_{iron} = Iron loss (W);
P_{loss} = Total loss (W);
Pr = Prandtl number;
$\dot{q}$ = Heat generation per unit volume (W/m^3);
R = Phase resistance (Ω);
R_e = Coil winding impedance (Ω);
Re = Reynolds number;

T = Temperature (K);
T_e = Electromagnetic torque (N m);
T_0 = The environment temperature (K);
U = Flow velocity (m/s);
u, v, w = x, y, z Directional velocity component;
V = Phase voltage (V); and
x, y, z = Cartesian coordinates (m).

Greek symbol

θ_r = Rotor salient pitch angle;
λ = Magnetic link (wb);
μ = Dynamic viscosity (Pa.s);
μ_t = The turbulent dynamic viscosity (Pa.s);
p = Density (kg/m^3);
σ_k = Turbulent Prandtl number of turbulent flow energy term;
σ_ε = Turbulent Prandtl number of turbulent energy dissipation rate;
σ_e = Electromagnetic field eddy current loss coefficient;
σ_h = Electromagnetic field hysteresis loss coefficient;
Φ = magnetic flux (wb); and
ω = r Rotor angular velocity (rad/s).

Subscript symbol

a = Phase a phase winding;
avg = Average value;
b = Phase b winding;
c = Phase c winding;
eff = Effective value;
f = Fluid;
in = Entrance;
L = Length of motor (m);
max = Maximum value;
min = Minimum value;
out = Exit;
s = Solid;
t = Turbulent flow;
x = Winding of different phase sequences (x = a, b, c); and
z = Measuring point on the surface of the motor casing.

1. Introduction

Nowadays, most of the systems, used in the development of electric vehicles, are hybrid electric systems. Most of the conventional motors are permanent magnet synchronous motors, which are characterized by high efficiency and high output torque. The permanent magnet motors contain permanent magnets that being exposed to heat at high temperatures significantly reduces their service life and rises maintenance difficulties (Bostanci *et al.*, 2017). A switched reluctance motor (SRM), which has the high efficiency of AC motor and low manufacturing cost, is proposed as an alternative for being used in hybrid electric vehicles. The SRM is a type of electric motor that runs by reluctance torque due to the delivered power to the windings in the stator; however, some sort of switching system is required to be used to deliver electric power to the different windings (Cabezuelo *et al.*, 2018). In SRMs, the power directly delivers to

the static coil windings, and hence, it results in notable simplification of these motors form the mechanical view. However, the requirement of the switching system increases the complexity of the electrical design. Nowadays, high-performance electronic devices are commercially available that can precisely perform the switching task between the windings in time, and hence, facilitating SRM configurations. In contrast, the switching of the electric power between the windings may results in torque ripple, which is the main drawback of SRMs where some controllers are also demanded to limit the torque ripple at low speeds (Nutan *et al.*, 2017). An excellent comparative review on both opportunities and challenges of SRM drives for electric propulsion is reported in (Bostanci *et al.*, 2017).

Although the complexity of electronic designs in SRMs has been increased, the elimination of mechanical moving parts increases the maintenance cost of the motor. In addition, the elimination of permanent magnets results in a reduction of the requirement of rare elements, and hence, it results in notable reduction of the production cost, which can cover the cost of the required electronic systems (Ohyama *et al.*, 2006). SRMs are capable of tolerating high-temperature operations and high-speed rotations. They can also work well in the applications with inferior conditions with vibration and impacts (Chiba, 2002). Because of the advantages of SRMs, these motors have become a feasible alternative to variable speed drive conventional motors in many applications (Li *et al.*, 2017). The application of SRMs has been increased not only in hybrid vehicles but also in washing machines, electric bicycles and vacuum cleaners. One of the important drawbacks of SRMs is the generation of waste heating during the operation. This issue gets critical in high power motors. The waste heat should be removed quickly from the motor body to prevent overheating. Thus, using an adequate cooling system for cooling of windings to maintain them in a safe temperature zone is one of the barriers for developing SRMs. Therefore, both modeling and optimization of these motors is an important key to their development and application. As mentioned, the heat is originated from the magnetic effects in the motor, and hence, the magnetic and thermal analysis of these motors are two inevitable parts of the design of SRMs, leading to complex multiphasic models. Literature review shows that there are important interesting attempts in modeling of the magnetic behavior and thermal analysis of SRMs. Two main ways to enhance the performance of SRMs are reducing the generation of waste heat and enhancing the cooling technique.

The reduction of waste heat generation requires the enhancement in the structural design of the magnetic fields. From the magnetic point of view, Chen and Gu (2013) have successfully used the finite element method (FEM) to study the overall structural design of the SRMs in a two-dimensional (2D) domain. Sundaram *et al.* (2009) studied the three-dimensional (3D) magnetic field of a SRM with two different pole configurations. They used the simulation software ANSYS to analyze the magnetic behavior of a SRM. Moallem and Ong (1990) examined the magnetic field of an SRM motor and reported that the grid quality is an important parameter on the accuracy of FEM predictions and has a large impact on the simulation results for prediction of torque and angle of an SRM. Kiyota and Chiba (2012) used FEM to simulate both types of the current mainstream motor permanent magnet synchronous motors and SRMs. These motors are commercially being used in electric vehicles. They found that at high speed, the output power of the SRM is 1.6 folds higher than the built-in interior permanent magnet synchronous motor, but the switching reluctance motor has 15-25 per cent more operating current and motor weight than the permanent magnet type. Li *et al.* (2017) performed an excellent survey on thermal modeling and design optimization of switched reluctance machines considering the mathematical modeling of the electromagnetic, the enhancement of the performances and thermal behaviors of SRMs. Diko *et al.* (2017) proposed a new concept of a three-phase 12/8 SRM with short flux-path and investigated the static and dynamic parameters and behavior of the motor for various operating conditions required for

vehicle applications. Yasa *et al.* (2018) addressed the power losses in high-speed switched reluctance machine. The power losses were the copper and iron losses in machine core; and switching and conduction losses in the drive circuit side. The results reveal that the skin and proximity effects increase the copper losses in high-frequency fed electric machines. In addition, iron losses are a significant portion of total electrical losses, but hard to compute. Moreover, both conduction and switching losses occur in power electronics switching devices in SRM drive circuit. The high-frequency switching can result in excessive switching loss levels.

In addition to the electromagnetic analysis of SRM, which seeks a solution to design a SRM with low loss, the cooling design of the motor is another important option, which can effectively take away the generated waste heat of the motor during operation. It should be noted that the waste heat generation is an inevitable part of any SRM that it can only be reduced through better designs. Hence, a good heat dissipation design enables the motor to operate efficiently in a safe state. Thus, a practical way to improve the performance of a motor is the enhancement of its cooling system. Abbasian and Jalali (2017) investigated the thermal behavior of a double stator SRM using FEM analysis. They used a 2D thermal model to reveal the actual heat distribution in components of the machine. Yu *et al.* (2017) investigated the electromagnetic and thermal characteristics of a canned SRM as a hydraulic pump drive. They reported that there is a fundamental difference between the thermal characteristics of an SRM and an ordinary machine due to considerable loss generated from the can shield in the air gap of SRM.

The present study aims to use a channel flow cooling system for cooling of SRM. Regarding the channel flow, Chamkha (2002) and Chamkha *et al.* (2002) have studied the mixed and free convection of a laminar flow in vertical channels. Al-Subaie and Chamkha (2003) have addressed the natural convection of particulate suspensions in a parallel plate channel. Various effect of heat transfer in a channel have been investigated in literature including the effect of channel boundary conditions (Chamkha, 2003; Chamkha and Al-Rashidi, 2010), developed flow (Chamkha *et al.*, 2003; Kumar *et al.*, 2010), magnetic field effects (Umavathi *et al.*, 2008; Chamkha and Al-Rashidi, 2013), radiation effects (Ahmed and Chamkha, 2014), conjugate heat transfer in thick walls (Umavathi *et al.*, 2016) and variable thermophysical properties (Rahman *et al.*, 2014).

Amorós *et al.* (2018) investigated the magnetic and thermal behavior of a double-sided linear SRMs to optimize the size of the motor under thermal and weight constraints. They coupled FEM analysis for magnetic propulsion force computation and a lumped parameter thermal network for thermal transient analysis. Ranjini and Murugan (2018) evaluated the electromagnetic performance of both types of conventional and SRM machines by FEM analysis. They also performed a thermal performance analysis using a lumped parameter model. For turbine generators with large amounts of waste heat, Zhe *et al.* (2009) compared air-cooled cooling systems (conventionally using air or hydrogen) with liquid-cooled cooling systems. The liquid cooling mainly involves closed circulation of a coolant (transformer oil or pure water) in pipelines. The results reveal that using liquid cooling involving evaporation phase change is capable of providing an even temperature distribution in the radial direction of rotor winding. Recently, Chiu *et al.* (2017) have modeled and simulated the electromagnetic field and thermal performance of a 30 kW SRM. They found that the maximum temperature in SRM cannot be reduced to a requested operating temperature with air cooling associated with mounted fins over the casing surface.

Review of available literature shows that most researches on SRMs have focused on the part of electromagnetic field analysis, mainly to improve the output performance of the motor itself, while the heat dissipation designs mainly used the estimation methods or lumped methods. Indeed, change in the magnetic structure of the new electric motors (from permanent magnets to SRMs) has increased the generated waste heat. Therefore, the

conventional cooling systems, which was used for permanent magnet systems, are not capable of providing adequate cooling power for safe operation of SRMs. The lumped models can only evaluate the average temperature in motor parts, but they fail to evaluate the temperature distribution and maximum temperature inside the motor components. Although the average temperature of a component is an important parameter, the local excessive temperatures in sensitive areas can fail or damage a motor. Hence, detailed 2D and 3D thermal models with the capability of evaluating temperature disturbance in a motor is highly demanded. The present study aims to model and analyze the electromagnetic field and cooling system of a high power SRM in the presence of a mounted fan at the rear of the motor. In the electromagnetic field analysis, the loss of the motor under running conditions, the copper and iron losses are considered according to different speeds. A 3D thermal model for thermal analysis of the motor is proposed. The actual distribution of the generated waste heat (evaluated from the electromagnetic field analysis) is imported in the thermal analysis of the motor. Furthermore, the thermal analysis is performed for both air-cooled and liquid-cooled cooling systems to meet the cooling demands of the motor.

2. Mathematical model

2.1 Physical model

This study aims to model the electromagnetic and thermal behavior of different parts of a real size SRM motor. Two important cooling systems of totally enclosed fan-cooled (TEFC) motor cooling and liquid-cooled cooling system are modeled and their characteristics are discussed in detail. To aim this purpose, the modeling of this work includes two parts as follows: electromagnetic field analysis and heat transfer analysis. Figure 1(a) depicts the schematic view of the SRM. The coil windings and the stator contact parts are schematically demonstrated in Figure 1(b). Figure 1(a) illustrates the motor front plane consisting of the casing, rotor, stator and shaft. The main components of the motor are the coil, the stator, the casing and the shaft. The SRM specifications are available in the related work of Chiu *et al.* (2017). These specifications are used for geometry construction and analysis of SRM.

To perform the electromagnetic and thermal analyses, both 3D and 2D models of SRM are established using SolidWorks drawing software. The electromagnetic field analysis of the motor is performed using JMAG-Designer software. The magnetic field of the motor is modeled using a 2D model. FEM method is used to perform the electromagnetic field coupling analysis. The electromagnetic field analysis includes the evaluation of the magnetic flux distribution, magnetic flux density and torque ripple of the motor and the loss of each part of the motor. The evaluated heat loss distribution of each component of the motor is then incorporated into the heat transfer calculations. The heat transfer analysis is performed using ANSYS-FLUENT software to obtain the temperature distribution of each component of the motor under different heat dissipation.

2.2 Electromagnetic analysis

The SRM uses a switching mechanism to deliver power to the different windings to produce reluctance torque. The basic mathematic equations in the form of differential equations for voltage, torque and mechanical equations, required for the analysis of the high power SRM, are represented in the following equations (Ranjini and Murugan, 2018; Chiu *et al.*, 2017):

$$V_x = i_x R_x + L_x \frac{di_x}{dt} + e_x \tag{1}$$

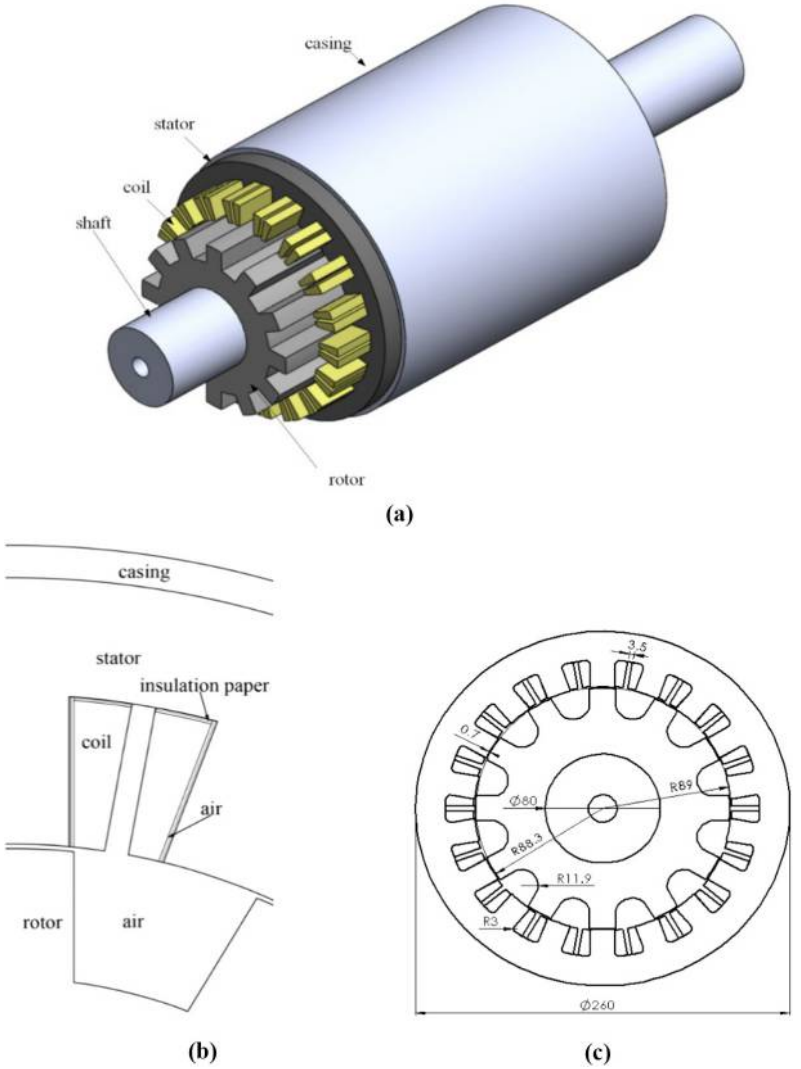

Figure 1.
The schematic view of SRM and the stator and rotor geometrical details; (a) schematic isometric view of SRM, (b) schematic diagram of the coil winding and stator contact parts, (c) motor front plan

$$T_e = \sum\nolimits_{x=a,b,c} \frac{1}{2} i_x^2 \frac{dL_{xx}(\theta_r)}{d\theta_r} \tag{2}$$

$$T_e(\theta_r, i_x) = J\frac{d^2\theta_r}{dt^2} + F\frac{d\theta_r}{dt} + T_L = J\frac{d^2\theta_r}{dt^2} + F\omega_r \tag{3}$$

where V_x is the voltage of phase x; T_e the motor torque; R_x is the resistance of coil winding for phase x; i_x is the current for phase x; e_x is the phase x counter electromotive force; and L_x

is the phase x coil winding section inductance. θ_r, F, J, T_L and ω_r denote the rotational angle of the motor, the friction coefficient of the motor with loading, the rotational momentum of the motor, the motor torque and the rotor angular velocity, respectively.

The main power losses of SRM are the copper loss (in coil windings), the iron loss (in core) and the mechanical loss (in moving parts), which are denoted by P_{copper}, P_{iron} and $P_{mechanical}$, respectively. The copper loss is Joule's loss, which is the result of the electric current through the wires of windings coil. This loss is evaluated as follow (Krishnan, 2001):

$$P_{copper} = R_e i^2 \tag{4}$$

where R_e and i are the resistance of wires coils and the current in the wires, respectively. The loss due to materials of stator and rotor is the iron loss (P_{iron}), which includes the eddy current loss (P_e) and the hysteresis loss (P_h). Eddy currents are loops of electric current, which are the results of a change in the magnetic field. Based on the Faraday's law, they are induced in conductors in planes perpendicular to the magnetic field and flow in close loops inside the conductor. In SRM, the eddy losses are the results of close loop currents in the magnetic core during the commutation period. The electrical energy loss due to the eddy currents transforms into a heat loss, which can be evaluated as follow (Ranjini and Murugan, 2018):

$$P_e = \sigma_e d^2 f^2 B^2 \tag{5}$$

where σ_e, d, f and B are the commutation frequency, eddy current constant, silicon steel thickness and the density of the magnetic flux. The hysteresis loss is the result of the required energy to change the orientation of the atomic magnets in the material of the magnetic domain due to the change of the magnetic field direction. The hysteresis loss (P_h) eventually transforms into the heat loss and can be evaluated using the following equation (Ranjini and Murugan, 2018):

$$P_h = \sigma_h f^2 B_{max}^2 \tag{6}$$

where σ_h denotes the hysteresis constant and the symbols of f and B have been introduced below the equation (5). The mechanical losses are mainly the results of friction of bearings and ventilation loss. The mechanical losses compared to the copper and iron losses are very small, approximately 1 per cent of total losses (Chiu *et al.*, 2017), and hence, these losses are neglected in the present study.

2.3 Thermal analysis

The SRM consist of solid parts such as the stator, rotor and casing and the fluid parts, which is either air-filled spaces or liquid coolant channel shells filled with water. The conduction heat transfer occurs in the solid parts. The parts containing either the air or a cooling liquid are subject to the convective heat transfer. Two general cooling approaches of both air-cooled and liquid-cooled designs are considered for the casing of the motor in the present study. The air-cooled system approach consists of natural convection cooling and forced convection cooling. The forced convection cooling is the result of a stable airflow over the motor casing because of the presence of a fan. The computational fluid dynamics (CFD) method is used to analyze the induced flow rate of the fan in various motor speed, i.e. fan speeds. The evaluated flow rates are used to evaluate the induced forced convective heat transfer coefficient over the motor casing. This way, the interaction between the motor

casing surface and the external air and development of the boundary layer over the casing surface is considered.

The airflow inside the motor using the TEFC modeled is also studied. It should be noted that the rotation of the rotor inside the motor induces a swirling distributed turbulence airflow in the casing. The turbulence flow enhances the heat transfer between the motor components and the air inside the motor. In addition, in a turbulence flow, the mixing between the air molecules inside the motor increases, and hence, it improves the heat transfer. The steady-state partial differential equation defining the flow and heat transfer in the parts of the motor containing either air or liquid are the continuity, momentum and the heat equations. These equations are as follows.

Continuity equation:

$$\frac{\partial u}{\partial x}+\frac{\partial v}{\partial y}+\frac{\partial w}{\partial z}=0 \tag{7}$$

Momentum equations in x, y and z directions:

$$\rho_f\left(u\frac{\partial u}{\partial x}+v\frac{\partial u}{\partial y}+w\frac{\partial u}{\partial z}\right)=-\frac{\partial p}{\partial x}+\mu_{eff}\left(\frac{\partial^2 u}{\partial x^2}+\frac{\partial^2 u}{\partial y^2}+\frac{\partial^2 u}{\partial z^2}\right) \tag{8a}$$

$$\rho_f\left(u\frac{\partial v}{\partial x}+v\frac{\partial v}{\partial y}+w\frac{\partial v}{\partial z}\right)=-\frac{\partial p}{\partial y}+\mu_{eff}\left(\frac{\partial^2 v}{\partial x^2}+\frac{\partial^2 v}{\partial y^2}+\frac{\partial^2 v}{\partial z^2}\right) \tag{8b}$$

$$\rho_f\left(u\frac{\partial w}{\partial x}+v\frac{\partial w}{\partial y}+w\frac{\partial w}{\partial z}\right)=-\frac{\partial p}{\partial z}+\mu_{eff}\left(\frac{\partial^2 w}{\partial x^2}+\frac{\partial^2 w}{\partial y^2}+\frac{\partial^2 w}{\partial z^2}\right) \tag{8c}$$

Energy equation in the fluid:

$$\rho_f C_{p,f}\left(u\frac{\partial T_f}{\partial x}+v\frac{\partial T_f}{\partial y}+w\frac{\partial T_f}{\partial z}\right)=k_{eff}\left(\frac{\partial^2 T_f}{\partial x^2}+\frac{\partial^2 T_f}{\partial y^2}+\frac{\partial^2 T_f}{\partial z^2}\right) \tag{9}$$

where u, v and w are the velocity vectors. The scalar variables of p and T_f are the pressure and temperature of the fluid, respectively. The thermophysical properties of $C_{p,f}$, ρ_f, μ_{eff} and k_{eff} denote the specific heat, the density, the effective viscosity and the effective thermal conductivity of the fluid, respectively. The effective thermal conductivity of the fluid (k_{eff}) is evaluated as $k_{eff} = k_f + c_{p,f}\ \mu_t/Pr_t$ where k_f is the thermal conductivity of the fluid, Pr_t is the thermal Prandtl of the fluid and μ_t is the turbulent dynamic viscosity of the fluid. The effective dynamic viscosity of the fluid is evaluated as $\mu_{eff} = \mu_f + \mu_t$ where μ_f is the dynamic viscosity of the fluid. The turbulent dynamic viscosity of the fluid is evaluated using $\mu_t = \rho c_\mu k^2/\varepsilon$ where k and ε are the turbulent kinetic energy and the turbulent kinetic energy dissipation rate, respectively. Here, $c_\mu = 0.009$ is a constant.

In the present study, k and ε are evaluated using the standard RNG k-ε model with standard wall function, which was proposed by Yakhot and Orszag (1986). This turbulence model is capable of dealing with the complex geometry flow paths and the vortex flow

fields. Therefore, the turbulence model of the RNG k-ε model is also incorporated in heat transfer analysis. The turbulent flow equations are as follows:

$$\frac{\partial}{\partial x_i}(\rho k u_i) = \frac{\partial}{\partial x_j}\left[\left(\mu + \frac{\mu_t}{\sigma_k}\right)\frac{\partial k}{\partial x_j}\right] + G_k - \rho\varepsilon \tag{10a}$$

$$G_k = \mu_t\left(\frac{\partial u_i}{\partial x_i} + \frac{\partial u_j}{\partial x_j}\right)\frac{\partial u_i}{\partial x_j} \tag{10b}$$

where G_k is the generation of the turbulent kinetic energy and σ_k is the turbulent Prandtl number of Turbulent kinetic energy. The turbulent diffusion equation is as follows:

$$\frac{\partial}{\partial x_i}(\rho\varepsilon u_i) = \frac{\partial}{\partial x_j}\left[\left(\mu + \frac{\mu_t}{\sigma_\varepsilon}\right)\frac{\partial \varepsilon}{\partial x_j}\right] - C_2\rho\frac{\varepsilon^2}{k + \sqrt{v\varepsilon}} \tag{11}$$

where σ_ε is the turbulent Prandtl number of turbulent kinetic energy dissipation rate, C_2 is the turbulent constant and υ is the momentum viscosity.

The energy equation for the solid parts is:

$$\rho_s C_{p,s}\frac{\partial T_s}{\partial t} = k_s\left(\frac{\partial^2 T_s}{\partial x^2} + \frac{\partial^2 T_s}{\partial y^2} + \frac{\partial^2 T_s}{\partial z^2}\right) + \dot{q} \tag{12}$$

where T_s denotes temperature distribution in the solid. The thermophysical properties of ρ_s, $c_{p,s}$ and k_s denote the density, the specific thermal capacity and the thermal conductivity of the solid. Here, $\dot{q}$ is the source term of heat generation, which comes from the heat losses in the motor. As mentioned, the heat losses are the copper loss, iron loss and the hysteresis loss, which are computed using the electromagnetic analysis of the motor.

Now, some boundary conditions are required for the above governing equations to be able to proceed with the numerical method. Some of the boundary conditions are related to the cooling approach used for cooling of the motor. In the present study, two cooling approaches that are air-cooled cooling system and liquid-cooled cooling system with various configurations are studied. As mentioned, a TEFC electric motor does not permit the ambient air to enter into the casing. The air is circulated inside the casing between the inner parts of the motor and casing.

Then, the casing body of the motor will be cooled by heat transfer with the ambient air. In this work, the cooling of the casing due to convection with the ambient air is modeled as a forced convection, which is the results of the air speed due to the fan power. Considering TEFC design model, air will be circulated inside the SRM between the inner components. The air inside the motor absorbs the generated heat from the stator and rotor and other components and gets hot. Then, the hot air reaches the inner surface of the casing and gives some of its heat to the casing. Then, the casing is cooled down using the forced convection air over its outer side or using cooling liquids.

The governing equations for the flow analysis are continuous and momentum equations as introduced in equations (7) and (8). The flow analysis is required for the thermal analysis of the motor using energy equations, equations (9) and (12). The motor

thermal performance analysis is carried out using the 3D model of the motor including its main components. To consider the rotating effects of the rotor on the flow and heat transfer inside the motor casing, the internal rotor is set to the rotating form while the other domains are stationary. In this way, the influence of the internal flow field on the thermal performance of the motor can be judged. Both the air-cooled and liquid-cooled cooling system designs are used on the outside of the casing. So that, the calculation of the flow field and energy equations are required in the solution process. The contact portion between the stator and the casing and the contact portion between the rotor and the rotating shaft follows the physic of heat transfer in solid. Regarding the SRM cooling using the liquid, the coolant liquid circulates in the motor casing through channels and removes the heat from the casing and the enclosed air inside the motor. For a TEFC–SRM, the boundary conditions for air cooling at the outer surface of the casing is the forced convection heat transfer. The boundary conditions for liquid cooling of the casing are as follows:

$$\text{Entrance}: \; u = u_{in},\; v = 0,\; w = 0,\; T = T_{in} \tag{13a}$$

$$\text{Exit}: \; p = p_{out} \tag{13b}$$

The inlet boundary condition is the flow velocity, and the channels are also small in diameter. Moreover, in practice, the flow would be circulated in a close loop, and indeed, the outlet of the channel is also a pipe connected to the cooling radiator and the pump, which have not been discussed in the present study. Hence, the specified pressure outlet is used as $p = p_{out}$ to solely specify a pressure drop:

$$\text{Solid} - \text{liquid interface at the channels walls}: u = v = w = 0,\; T_f = T_s, -k_f \frac{\partial T_f}{\partial n} = -k_s \frac{\partial T_s}{\partial n} \tag{13c}$$

This boundary condition is used two times as given below. The equation (13d) is the conjugate heat transfer between the solid casing of the motor and the air inside the casing. The equation (13e) is the heat transfer between the liquid coolant in the channels of the casing and the solid metal of the casing:

$$\text{Contact surface between the casing and motor}: \; -k_{s_1} \frac{\partial T_{s_1}}{\partial n} = -k_{s_2} \frac{\partial T_{s_2}}{\partial n} \tag{13d}$$

$$\text{Other walls and symmetric interfaces}: \; \frac{\partial T_s}{\partial n} = 0 \tag{13e}$$

Outside the casing, an array of extended surface, fin heat sink, can be embedded to increases the thermal interaction with the ambient air and the casing metal. A fan can also be used to increase the flow velocity over the outer surface of the casing. The fins can be arranged in special way to make some airflow passages. Thus, in the case of air-cooled RSM, the casing can be either cooled with the natural convection or forced convection using the ambient air.

In this case, the heat transfer between the ambient air and the casing surface or fins can be evaluated using the convection heat transfer as follow:

$$-k_s \frac{\partial T_s}{\partial n} = h_{ambient}\left(T_{s,out} - T_{ambient}\right) \tag{13f}$$

where $h_{ambient}$ is the convective heat transfer coefficient between the outer surface of the casing and the ambient airflow and $T_{s,out}$ is the temperature of the outer surface of the casing. Here, n is the normal vector of the surface and T_s and k_s were introduced in equation (12).

To solve the governing equations, equations (7) to (12) are associated with the corresponding boundary conditions, equation (13), the thermophysical properties of the fluids and motor components should be available. The thermophysical properties are available in the previous study (Chiu *et al.*, 2017).

3. Numerical method

A 3D model of a high power SRM containing cooling channels and fins is established with computer-aided design software, SolidWorks. The necessary heat sources are obtained by evaluating the important motor losses (copper and iron losses) from the electromagnetic field analysis. The JMAG-Designer software is used to evaluate the heat loss and the motor performances. Then, the fast Fourier transform is used to transfer the evaluated motor loss to the thermal analysis for the study temperature distribution in the motor components.

The casing is analyzed in various cooling scenarios with a different arrangement of fins and liquid cooling channels. Furthermore, in the casing shell, a snake shape channel is designed for water flow circulation and study the effect of liquid cooling. The working fluid in the channels is pure water. The commercial software, ANSYS-Fluent, is used for thermal analysis. The finite volume method and SIMPLE (Semi-Implicit Method for Pressure-Linked Equations) algorithm for pressure–velocity are used. The flow field in couple with the energy equations are used to evaluate the contours of temperature distribution in motor components and especially coil windings. The performance of the cooling mechanism is judged by the study of maximum temperatures of the coil windings. In the electromagnetic and thermal analyses, the SRM with its real dimensions is studied. The insulation material and the wires in coil windings are assumed to be uniform for geometrical and computational simplification. To solve the governing equations, the grid points were generated to discrete the domain into computational subdomains. As mentioned, the heat transfer and fluid flow calculations are performed using the finite volume method. The second-order upwind scheme for both of the velocity and the temperature fields was used to increase the accuracy of the solutions. Finally, for the numerical analysis, the residual value of the numerical calculations is set to 10^{-3} for the continuity and momentum equations and 10^{-6} for heat equation. Hence, the numerical accuracy of the operation result is ensured under the above conditions.

The electromagnetic field loss of the SRM occurs in the form of heat during operation, so the loss in operation should be taken away to ensure that the motor operates under safe conditions and the temperature of the coil winding is controlled on the winding surface insulation material. Figure 2(a) depicts the conceptual schematic of an air-cooled system using a fan mounted on the shaft, which forces the ambient air to follow over the casing and embedded fins at the outer surfaces of the casing. Figure 2(b) presents the geometry and dimensions of the used fan blades. In this work, two liquid-cooled cooling system approaches inside the casing are used and schematically shown in Figure 3. Figure 3(a)

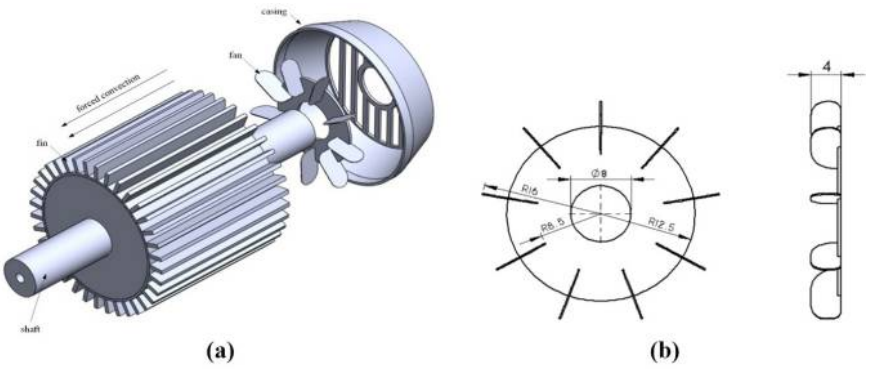

Notes: (a) The SRM and its outer casing surface; (b) front and right-side plan of the utilized fan

Figure 2. The air-cooled cooling system conceptual isometric view

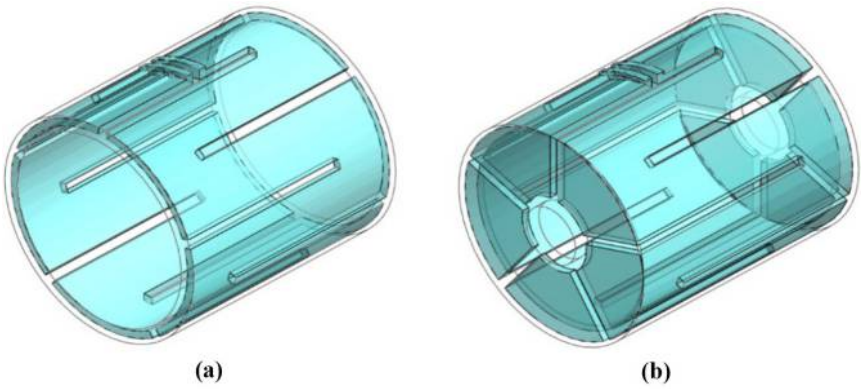

Notes: (a) Channel shell; (b) extended channel shell

Figure 3. An isometric view of the liquid cooling shell

depicts the cooling shell with snake-shape channel flow paths, referring as channel shell and Figure 3(b) demonstrate the extended cooling shell with the snake-shape flow path, which covers the front and back panels of the motor, referring as extended channel shell. Indeed, in extended channel shell design, the internal cooling acts as a liquid jacket for the stator and other parts of the motor. The geometrical specification of the liquid cooling design is reported in Table I.

The combination of both liquid-cooled and air-cooled cooling systems as a hybrid cooling system is shown in Figure 4. This figure depicts a fundamental schematic view of a hybrid of the liquid-cooled system with the natural convection cooling [Figure 4(a)] and forced convection cooling using a fan [Figure 4(b)]. As seen, in all of the fan-cooled configurations the fan is mounted on the motor shaft, and hence, the rotational speed of the fan is proportional to the rotational speed of SRM. As mentioned before, the airflow rate over the casing is evaluated using the rotational speed of the fan in a separate flow analysis in the

present study. Later, the convective heat transfer coefficient is evaluated using the airflow rate data and used as a convective thermal boundary condition over the outer surface of the motor casing and the mounted fins. The schematic view of the used model for evaluating the flow rate of the ambient flow over the motor casing is depicted in Figure 5. The fluid enters the fan housing and then moves over the casing surface by developing a hydrodynamic boundary layer. The large cylindrical domain in Figures 5(a) and (b) denotes the ambient air under the effect of the fan and the airflow. This domain is considered big enough to represent the quiescent ambient air. The fluid flow velocity over the casing is measured at the point Z_L. As mentioned, later, this velocity is used for the evaluation of the convective heat transfer over the casing surface as a boundary condition. The cooling fan induces a forced flow convection on the outer surface of the motor casing.

The flow path inlet is designed to have the same diameter as the outer cover of the fan when installing the cooling fan. In practice, the cover ensures that the fan is not disturbed by foreign objects, causing the fan to jam or the motor to operate abnormally. The outlet is adopted as a large domain to model the ambient air surrounding the motor. The motor casing is modeled as a plate. The fan is placed in the flow channel through the CFD analysis software ANSYS-FLUENT. Using the solution of the flat flow, the free flow velocity is computed next to the surface of the outer casing and the convective heat transfer coefficient over the casing surface is calculated using the following boundary layer equation (Bejan, 2013):

Table I.
Fully enclosed fan cooling (TEFC) design model specification sheet and the channel shell design

Specification	Value	Specification	Value
Inlet channel diameter (mm)	360	Outlet channel diameter (mm)	800
Inlet length (mm)	200	Exit channel length (mm)	600
Cooling fan outer diameter (mm)	300	Cooling fan inner diameter (mm)	250
Fan blade height (mm)	37	Number of fan blades	9

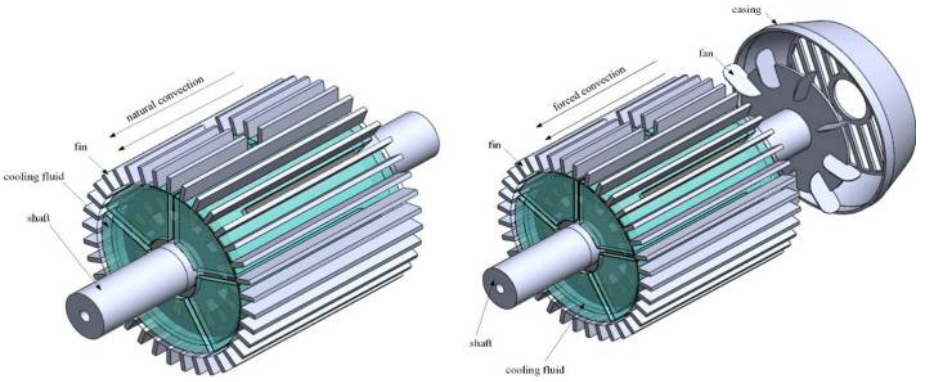

Figure 4.
Schematics of liquid-cooled air-cooled cooling system isometric view

Notes: (a) Natural convection cooled system; (b) air-cooled liquid-cooled hybrid cooling system

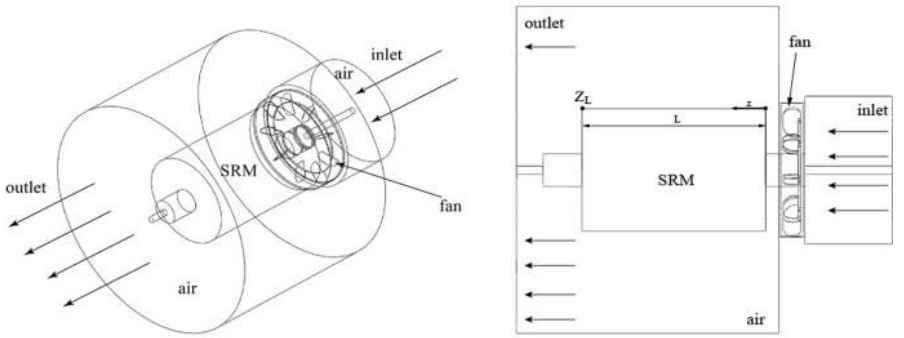

Figure 5.
Fully enclosed fan cooling (TEFC) design model

Notes: (a) Angular view; (b) schematic diagram of the air flow velocity measurement point at Z_L

$$h_z = 0.332 \frac{k_f}{L_z} \sqrt[3]{Pr} \sqrt{Re_z} \tag{14}$$

where h_z is the local convective heat transfer coefficient. Here, k_f and Pr denote the thermal conductivity and air Prandtl number, respectively. Re_Z is the airflow Reynolds number as $Re_Z = \rho_f U_Z Z / \mu_f$ where U_Z is the free stream flow velocity.

To find a sufficient cooling design for the selected SRM, various combination of cooling geometry and cooling methods are analyzed. The steps of the design procedure are summarized in the flow chart of Figure 6. As seen, the geometry of the SRM is built, and then, the electromagnetic and thermal analysis are commenced. The electromagnetic analysis is performed for evaluating the loss distribution, magnetic field distribution, magnetic flux and torque ripple. The loss distribution is passed to the thermal model. The thermal analysis is performed for both of the air-cooled and liquid-cooled approaches. The air cooling includes the natural convection, forced convection and various fin configurations. The liquid cooling involves thermal analysis for two types of channel shells and various combination of liquid-cooled with natural convection and fins. Finally, the thermal analysis is performed for the hybrid liquid-cooled and air-cooled forced convection with fins. The temperature range that can be withstood by insulation material in motor windings is another important issue in the safe operation of an SRM. When the insulation material melts, it may cause the winding to be short-circuited and burned. In the present study, the selection of the insulation material is based on the Chinese National Standards (CNS) data. It is stated that the insulating materials can be divided into seven grades according to temperature resistance, such as Y, A, E, B, F, H and C (Chinese National Standard, 2018), as shown in Table II.

The configuration of the grid size in the study can be divided into two parts, namely, electromagnetic field analysis and heat transfer analysis. In the electromagnetic field analysis, attention is paid to the distribution of the magnetic lines and the magnetic flux density. For the electromagnetic analysis, the grid size of 0.1 mm is used to ensure a dense sufficient grid for accurate calculations. The grid is automatically generated by the rotation periodic mesh generation approach and the appropriate peripheral air grid size is adjusted so that the calculations can be performed fast and accurate. As the electromagnetic field

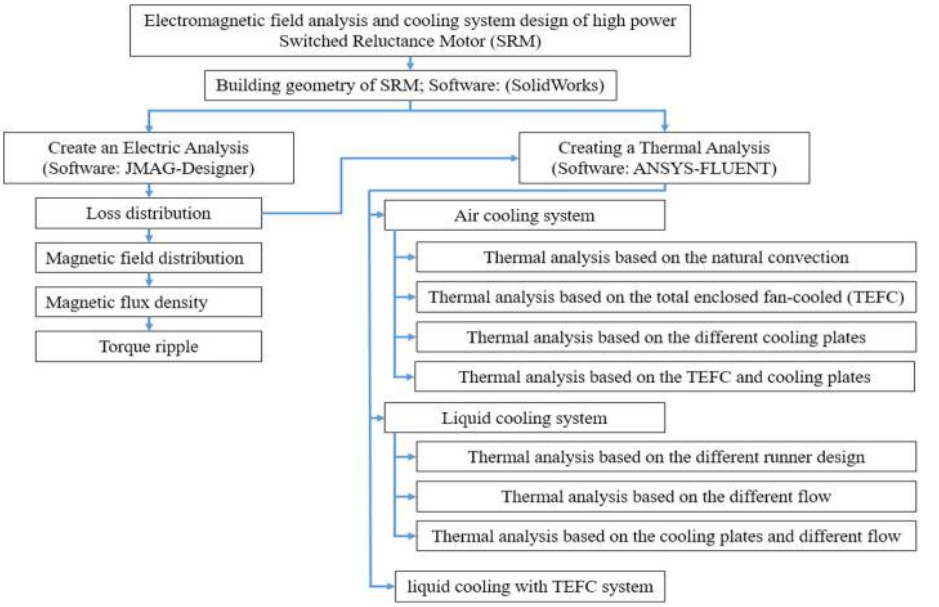

Figure 6.
Flow chart of the research analysis

Table II.
Rating table of Chinese national standard of electrical insulation materials (Chinese National Standard, 2019)

Insulation class	Maximum allowable temperature (°C)	Maximum allowable temperature rise (°C)
Y	90	105
A	105	120
E	120	130
B	130	155
F	155	180
H	180	200
C	180 and above (depending on the properties of the insulation material)	200 and above (depending on the properties of the insulation material)

analysis is calculated using a 2D model, the mesh is an unstructured triangular mesh. The mesh nodes of the air gap domain, which is placed between the rotor and stator, should be joint with the mesh grids of the rotor and stator. Thus, the mesh of the narrow air gap is under the influence of its adjacent domains. Hence, the dimension of the inner air gap grid sideline is set to 0.4 mm to produce accurate results for the magnetic flux distribution and the magnetic flux density calculations. Therefore, by using this fine grid, the switching loss of the SRM at different rotational speeds is obtained accurately.

In the heat transfer analysis, the part of the motor that rotates the air-fluid in contact with the rotor is meshed as boundary layer scheme whit size of 2.0 mm. In the boundary layer grid scheme, the grid is dense next to the surface, and then, density of the grid decreases by the increase of the distance from the surface. This way the grid can effectively capture the large gradients next to the surface. The coil winding and the fluid parts are meshed using

structured mesh with size of 3.0 mm. The rotor, stator, casing and shaft parts are mainly subject to direct solid heat transfer, and hence, a larger mesh size of 5 mm is used. The internal air is affected by the rotating flow field so the mesh size is set to 3 mm. In the overall model mesh setting, the context of the global parameter setting is set to a high quality to decrease the skewness of the mesh and increase the mesh quality at the boundaries. In the second part of the fully enclosed fan cooling system model, the mesh size of the fan rotating fluid is set to 2 mm. The inlet and the outlet flow channel are set to a structured mesh with the mesh size of 10 and 8 mm, respectively. The boundary layer setting is added to the surface of the motor casing in the flow channel, to effectively capture the velocity distribution inside the channel.

The grid independency tests of this research model can be divided into two parts. The first part is the grid independency analysis of the electromagnetic analysis of the SRM model. The mesh size of the coil winding and the working fluid are observed for important parameters. Three grid sizes are selected for the model and the results are studied. Grids A, B and C with the mesh sizes (total mesh size) of 2 mm (7,529,119), 3 mm (5,248,656) and 3.5 mm (4,595,430), respectively are used to perform a grid analysis. The calculation was performed using the grids A, B and C for the motor speed 4,000 rpm, the ambient convection heat transfer coefficient (h) 5 W/m^{2}K and the working fluid of liquid water. The calculation results for the temperature are reported over a line, A-A, in the interior section of the motor. The interior section along with the line A-A, which is illustrated in red, is depicted in Figure 7. Line A-A is taken along the Z-axis direction, which can be specified using the two points with the coordinates of (−10 mm, 100 mm and 0) and (−10, 100, and 280 mm). Figure 8(a) shows the temperature as a function of distance along A-A for three selected girds of A, B and C. The corresponding highest and lowest temperatures along this line at different motor components are reported in Table III. The results show that the relative temperature error between the results of very fine Grids A and B is less than 2 per cent. Hence, Grid B is selected for the future calculations. The second part is the analysis of the grid independency of the flow of the ambient air because of the fan. The calculations results of this part are required to obtain the external flow velocity. This flow velocity will be used in the air-cooled thermal analysis of the motor as a force h over the outer surface of the motor casing. Therefore, this model only calculates the external air velocity of a fan at each of the motor speeds.

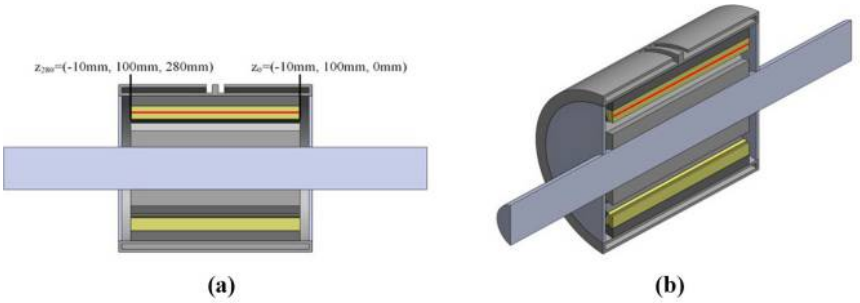

Notes: (a) Establishing a straight line on the YZ plane; (b) changing the distance along the Z axis

Figure 7.
Schematic diagram of the straight line on the coil winding for the grid independency analysis

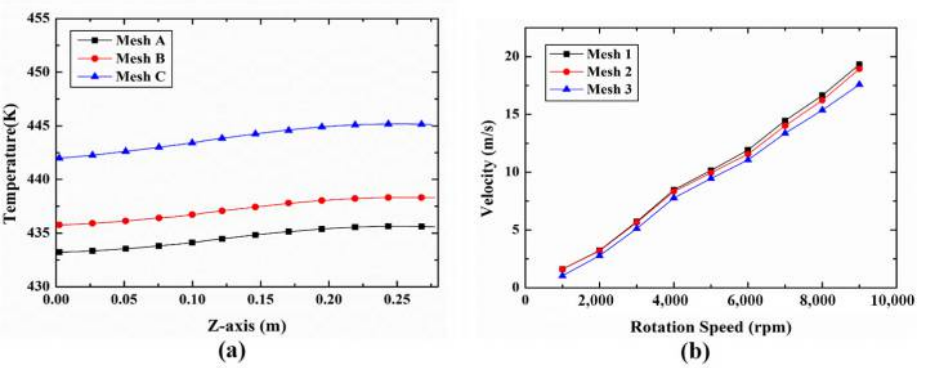

Figure 8.
The grid independent tests

Notes: (a) The evaluated temperatures for test grids of A, B and C; (b) predicted air velocity at point U_L as a function of the rotational fan speed and for the three meshes 1-3

Table III.
Grid independence analysis of the maximum and minimum temperatures (K) of the motor components under different grids

	Coil temperature		Stator temperature		Rotor temperature	
Grid	Maximum	Minimum	Maximum	Minimum	Maximum	Minimum
Mesh A	444.4	421.1	388.1	339.8	456.8	436.9
Mesh B	448.0	424.8	390.2	345.9	460.9	441.0
Mesh C	454.6	430.2	396.4	352.1	467.1	447.3

Three different grids, namely, Mesh 1, Mesh 2 and Mesh 3, with different sizes are produced to study the effect of the grid size on the flow rate on the surface of the casing. The size of the rotating fluid domain and the rear channel mesh and the boundary layer mesh of the casing wall are considered as the control parameters of the mesh. The size of the rotating fluid domain and the channel are adopted as 2 and 12 mm, respectively. The total number of boundary layers is adopted as eight layers. This configuration produces a grid with the total mesh size of 7,551,153 meshes. For Mesh 2 (Mesh 3), the size of the rotating domain, the channel and number of boundary layer layers are set to 2.5 (2.8), 15 (20) and 5 (3) mm layers. These grid configurations result in the total mesh sizes of 4,795,121 for Mesh 2 and 3,011,540 for Mesh 3. Using the produced grids, the calculations are performed for the flow and thermal analysis with normal inlet and outlet pressure and temperature boundary conditions.

To study the effect of the grid size on the results, the fluid velocity is reported at U_L. This point, which is placed at the edge of the boundary layer and above the point Z_L, is depicted in Figure 6(b). The air velocity at point U_L for the Meshes 1-3 and various rotational fan speed is measured and plotted in Figure 8(b). This figure depicts that Mesh 2 results in a relative error less than 3 per cent, and hence, Mesh 2 is adopted of the calculations of this part. This figure also shows that the air speed is 1.6 m/s when the rotational speed is 1,000 rpm and the air speed is as high as 18.9m/s when the rotational speed is 9,000 rpm.

4. Results and discussion

In this work, the electromagnetic field analysis software JMAG-Designer is used to calculate the loss of each component of the high-power SRM under running condition, and then the CFD software ANSYS-FLUENT is used to analyze the cooling system of the motor, thereby ensuring that the motor can be operated safely and efficiently. Therefore, this section can be divided into two major parts. The first part is the analysis of the motor loss under operation. The motor is running at the various speeds and the loss of the internal components of the SRM is computed. The evaluated losses are transformed into heat to be imported into the flow and thermal analysis design. The second part is the cooling system design, using the fully enclosed fan cooling design, the motor casing covered with fin design, the liquid-cooled flow channel shell design, the liquid-cooled with fan-cooled design (hybrid cooling design).

4.1 Motor running loss

Using the magnetic field analysis, the heat loss generated in the coil winding, stator and rotor at each speed can be evaluated. Mainly, the loss in the coil winding is the focus of this research study, because the temperature of the coil winding increases as the heat loss in this component increases. If the temperature of the coil winding exceeds the allowable temperature of the surface insulating material, the motor fails to operate. Figure 9 shows the losses of the coil, stator and rotor at various motor speeds. This figure shows that the loss of the coil winding reaches to the maximum value of 932 W at the motor speed of 4,000 rpm. This large magnitude of loss is mainly because of the large required current of the motor at this commutation frequency and current. From equation (4), it is clear that the loss is proportional to the square of the current, so the high value of a current results in a large loss in the coil winding. As the rotation speed increases, the motor commutation speed becomes faster, the excitation time of each phase sequence is shortened and the loss in the coil winding is also small. However, as the commutation frequency increases, the iron losses in the stator and the stator are greatly increased. Based on equations (5) and (6), the magnetic hysteresis and the eddy current losses are proportional to the commutation frequency squared. Thus, mainly at a high rotational speed, the iron loss is higher than the copper loss. As seen in Figure 9, the rotor and stator losses climb as the motor speed increases. As

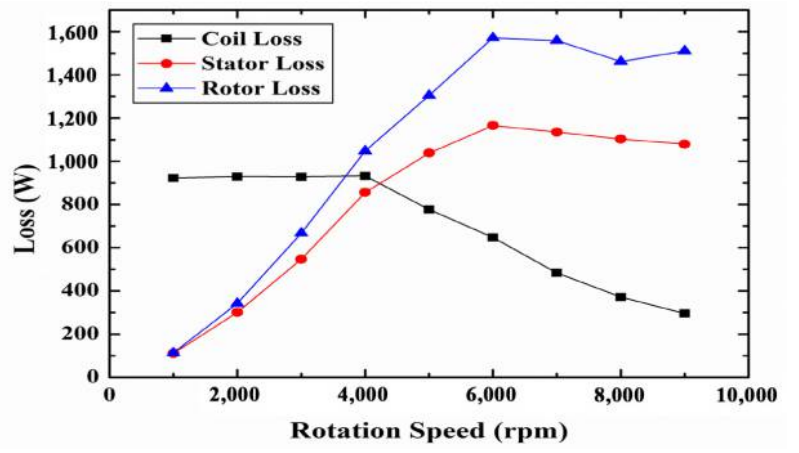

Figure 9.
Loss of motor components at different motor speeds

mentioned, the copper loss is very important in SRM as it may damage the coil winding due to overheat. Hence, to ensure that the motor operates under safe conditions, the temperature of the coil winding is predicted to be the key to the selection of motor insulation when the speed is 4,000 rpm. As a result, in the present study, the heat dissipation analysis is carried out with reference to the loss value of each component at 4,000 rpm.

4.2 Analysis of air-cooled cooling system

As the center of the cross-section of the SRM the highest temperature profile occurs. This cross-section is referred as section A-A. The temperature distribution of this cross-section is used a temperature distribution map to understand the temperature distribution inside the motor under various cooling systems designs in future analysis of this study.

As the first case, it is assumed that the convective heat transfer effect occurs under natural convection in the well-ventilated natural environment, and there is no fan installed at the back of the motor and also the casing surface is flat with no installed fin. In this case, the natural convection coefficient is assumed in the practical range of 5-25 W/m^2K (Mills, 1999). The temperature distribution is evaluated at the reference speed of 4,000 rpm for each convective heat transfer coefficient. At 4,000 rpm, the coil loss, the stator loss and the rotor loss are 932, 856 and 1,048 W, respectively. These losses are incorporated as the thermal source terms in the thermal analysis of the motor. The results of thermal analysis show when the natural convection heat transfer coefficient (h) of the motor is 5 W/m^2K, the highest temperature on the coil winding is 1,305.0°C. It is found that the increase of the convective heat transfer coefficient significantly reduces the temperature distribution inside the motor components. By the increase of the convective transfer coefficient (h) to 10 W/m^2K, the maximum temperature on the coil winding is reduced by 610°C, which is about 46.7 per cent compared with the convective heat transfer coefficient of 5 W/m^2K. The increase of the natural convection heat transfer coefficient from 5 to 15 W/m^2K dramatically drops the temperature of the motor components; however, the rate of the temperature drops with the future increase of h decreases and the amplitude gradually becomes flat and an asymptotic trend of behavior can be observed. When the convective heat transfer coefficient is low ($h = 10$ W/m^2K), the thermal resistance of the convective heat transfer is the dominant thermal resistance of the system, and hence, a small decrease of this resistance results in large temperature changes.

When the ambient convection heat transfer coefficient is 25 W/m^2K, the highest temperature at the coil winding is 321.3°C. At this time, the temperature is still higher than the maximum temperature allowed by the standard of the insulation material. Thus, larger values of h are required to further decrease in the temperature of the motor components. It should be noted that the natural convection of the environment is not stable, and in many environments and motor installation positions, it can be suppressed. Therefore, it is necessary to develop a fan cooling design by means of a fan to provide a stable airflow over the casing surface. This stable airflow produces a stable convective heat transfer coefficient on the motor casing surface. In addition, the increase of the heat dissipation area of the surface of the motor casing, which is in contact with the airflow another option for the enhancement of the cooling system. Thus, using heat sinks can enhance the heat transfer from the motor casing.

The airflow that is designed to flow stably on the surface of the air-cooled heat dissipation system is the most important factor affecting the cooling system. However, the natural convection is uncontrollable and may change drastically with the motor installation environment. Therefore, this study uses a fully enclosed fan cooling system to install a fan on the motor shaft to generate a stable flow field on the surface of the casing.

The effect of the rotation speed on the flow velocity of a mounted fan was discussed in Figure 8(a). The obtained flow profiles are used to evaluate h at the casing surface using equation (14). Here, using the results of Figure 8(a) and equation (14), the values of h have been calculated and reported in Table IV. Motor losses were also reported in Figure 9. This figure demonstrates that the loss is mainly distributed on the rotor and stator at high speeds. However, at high speed, the forced convection coefficient (h), which is the result of rotational speed of the fan, increases. At low speeds of the motor, copper loss is high in the coil and the forced convection heat transfer coefficient is also low due to the low speed of the fan. Hence, whether the convective heat transfer coefficient generated by forced convection in low speeds is capable of effectively remove the heat of the coil is an important key factor in the air-cooled cooling system design.

Based on the results of Table IV, in the case of 1,000 rpm motor speed, h is 9W/m^{2}K, so the result of the natural convection heat transfer coefficient of 5 W/m^{2}K can be used as the original state of the study without the presence of a cooling system design, mainly because of the natural convection-based environment. It should be noted that the convective heat transfer of 1,000 rpm due to the fan is a stable heat transfer flow. To understand the effect of the presence of the air-cooled cooling system on the motor temperature at different speeds, the losses of the motor components, i.e. Figure 9, are matched with the forced convection heat transfer coefficient, reported in Table IV, at each speed. Then, the thermal analysis of the motor component is performed. The results show that the coil loss is much higher than the stator and rotor losses when the speed is 1,000 rpm, so the highest temperature on the coil winding is 361.1°C. As mentioned, Figure 9 shows that the peak value of the coil loss is reached at the speed of 4,000 rpm. It is also found that at the speed of 4,000 rpm the maximum temperature of the coil reaches to 656.4 K (383.3°C). As the motor speed increases, the commutation frequency increases and the copper loss generated in the coil winding decreases. Hence, the maximum temperature in the coil winding drops to 266.7°C when the speed is 9,000 rpm. Although the temperature coil winding drops to 266.7°C, the maximum temperature of the coil winding is still 383.3°C at 4,000 rpm, which is still too high to be tolerated by the standard insulation material. Therefore, to further enhance the heat dissipation, heat sink fins are used to increase the heat dissipation area of the surface of the casing and assist the motor cooling.

Various configuration of fins over the motor casing are studied. The maximum temperature of the coil windings under the same total heat dissipation area is compared to find the optimum height and width of the heat sink fins. Different numbers of heat sink fins are mounted on the motor casing using the optimal fin shape design. During the analysis,

Motor speed (rpm)	Airflow speed (m/s)	h (W/m^{2}K)	Coil windings maximum temperature			
			Re = 500	Re = 1,000	Re = 1,500	Re = 2,000
1,000	1.60	9	382.6	370.3	366.1	362.1
2,000	3.18	12	392.0	375.9	372.9	368.0
3,000	5.65	16	403.2	386.7	380.5	375.3
4,000	8.32	20	416.3	396.7	390.3	384.5
5,000	9.95	22	412.5	394.3	385.4	380.3
6,000	11.56	24	407.0	391.9	383.5	377.9
7,000	14.02	26	394.5	379.5	372.2	367.4
8,000	16.23	28	381.9	367.8	362.7	358.5
9,000	18.94	30	375.5	363.8	358.2	354.2

Table IV. The maximum temperature (K) of the coil windings for the hybrid heat dissipation design of air-cooled and liquid-cooled extended shell for various flow rates

the ambient convection heat transfer coefficient is set to 5 W/m^{2}K, which corresponds to the natural convection heat transfer, and the speed of the motor is considered as 4,000 rpm.

Various heat sink fin size, width and numbers are tested for a fixed motor casing diameter. The fin heights of 20, 30, 40 and 60 mm, fins with the width of 2, 4 and 8 mm and fin numbers of 16, 26 and 36 are tested by evaluating the maximum temperature of the motor components. The results show, as the fin width or the number of fins increases, the maximum temperature on the coil winding decreases. However, it should be noted that increasing the width of the fins or their numbers reduces the width of the airflow passages. The narrow flow passages can block the airflow ways, which limits the flow speed and consequently the convective heat transfer. Therefore, the heat sink with 36 fins of height of 30 mm and width of 8 mm is selected as optimum heat sink fins. The optimum heat sink drops the maximum temperature to 563.3°C under the natural convection (h = 5 W/m^{2}K). This temperature is still too high for the standard insulation materials. It should be noted that using a large number of fins would decrease the width of the flow passages that should be avoided. In the future thermal analysis results, only the optimum heat sink will be used.

The maximum temperature of the motor components is also studied for various motor speeds when there is a mounted fan at the rear of the motor with the heat sink. The fin design effectively increases the heat exchange area between the motor and the air and improves the performance of the cooling system. Figure 10 shows the temperature contours inside the motor components at the cross-section of A-A at various motor speeds for a motor with fan and heat sink (36 fins of height 30 mm and width 8 mm). The results show that the maximum temperature of the motor at the coil windings is 197.9°C for the motor at the rotational speed of 4,000 rpm. Although the evaluated temperature is not within the limits of insulation standard grades, it is close to the H-class 180°C of the insulation material temperature grade published by the CNS National Bureau of China. It is worth noticing that the rotational speed of 4,000 rpm corresponds to the maximum coil loss. It is also found that the maximum temperature of the coil windings at high speeds of 8,000 and 9,000 rpm drops to 152.3°C and 142.8°C, respectively. These temperatures are at the range of 155°C corresponding to the insulation grade F.

The analysis of the air-cooled cooling system using fins and a fan shows that the best air-cooled cooling system can take away the most of heat losses. The maximum temperature of the coil winding is still higher than the temperature resistance of the insulation material published by the National Bureau of Standards. Mainly, the reason for the high temperature of the motor is due to the fact that it is completely enclosed. The design of the motor structure can prevent dust and moisture from entering the motor and increase its service life. However, the internal air is separate of the ambient air, and hence, the direct convection heat transfer with the surrounding air is not possible. The air inside the motor can only be rotated by the rotor to form the internal flow field and make internal convection heat transfer with the stator, rotor and the coil windings and get hot. The hot air also makes a convection heat transfer with the motor body, and then the external air-cooled cooling system is used to carry heat away from the motor body.

In cases in which the motor is operating under various operations and speeds, the air-cooled system with fan and heat sink can be normal and safe. However, it cannot work stably in any rotation speed, e.g. 4,000 rpm. Hence, further developing of the cooling system is essential. To aim this purpose, a liquid-cooled cooling system is designed to ensure efficient operation of the motor at all speeds and in different environments. The liquid-cooled cooling system uses water as the working fluid. Two designs for the liquid-cooled cooling system are proposed. One is a snake-shaped channeled shell, which only covers the surface of the motor casing, referring as channel shell. The other one is designed to be a

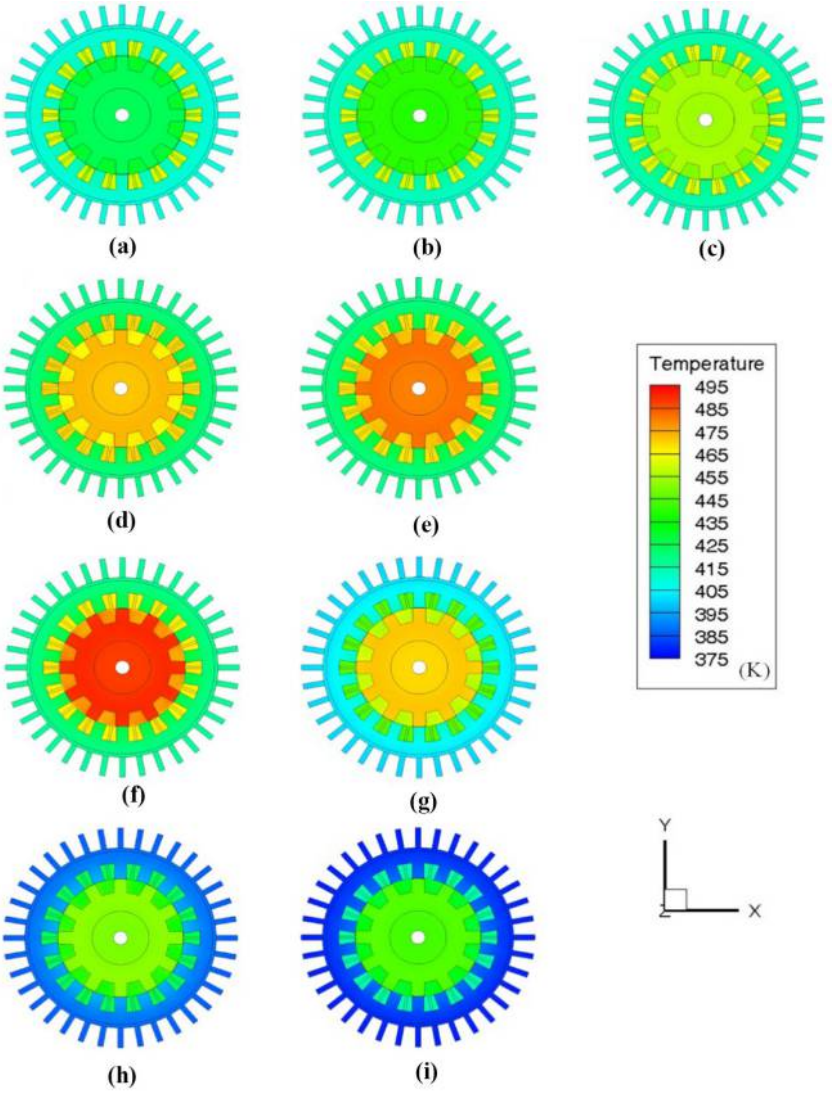

Notes: (a) 1000 rpm; (b) 2000 rpm; (c) 3000 rpm; (d) 4000 rpm; (e) 5000 rpm; (f) 6000 rpm; (g) 7000rpm; (h) 8000 rpm; (i) 9000 rpm

Figure 10.
The temperature distribution contours in motor components at various motor speeds with fan and heat sinks

snake-shape channeled shell, which is extended to the front and rear cover plates of the motor, referring as the extended channel shell, to increase the heat transfer area between the working fluid and the motor casing. To perform the thermal analysis, the convective heat transfer coefficient of the surface of the casing is set to 5 W/m^2K, which is corresponding to the natural convection. The maximum temperature of the motor components for various values of Reynolds number of coolants in two types of the channel shell and extended

channel shell is studied when $h = 5$ W/m^{2}K. The effect of the presence of optimum heat sink fins is also studied.

Figures 11(a) and 12(b) show the temperature distribution of motor for the channel shell and extended channel shell liquid cooling, respectively when the motor speed is 4,000 rpm and Re = 500. In the absence of fin and under natural convection cooling ($h = 5$ W/m^{2}K) the thermal analysis results show that the maximum temperature of the rotor is 187.8°C (460.9 K) when the outer casing is equipped with channel a shell. The highest temperature of the coil windings, which is most of the concern, is 174.9°C (448.0 K). According to the classification of national standard insulation material, the insulation material grade can be used with the maximum allowable temperature of 180°C. Figure 12(b) illustrates the temperature distribution of the motor components for the case of an extended channel shell. This figure demonstrates that the coil winding is the highest temperature component of the motor interior, and the temperature is 166.5°C. Compared with the temperature distribution of the channel shell, the extended channel shell shows an increased heat transfer capacity. This is due to the increase in the contact area between the working fluid and the casing; so, the maximum temperature of each component is lower than that of the channel shell cooling system. As the heat exchange area between the working fluid and the casing increases, the flow path also increases, which results in the improvement of the cooling system. However, considering a fixed working fluid flow rate, the increase in the length of the cooling channel results in the increase of the pressure drop. The increase of the pressure drop leads to an increase in the power consumption of the pump for circulating the coolant water.

The results show that when the working fluid with Re = 500, the pressure loss of the extended channel shell flow is 1.17 folds of the channel shell flow, but the maximum temperature of the coil winding can be lowered by 8.4°C. It can also significantly reduce the maximum temperature of the rotor by 32.9°C. Indeed, by using the flow extended channel shell cooling system, in which its channels are extended to the front and rear cover of the motor, the waste heat transferred from the rotor to the shaft is effectively carried away from the motor body by the flow of working fluid. Thus, the pump needs more power consumption, but it has a better cooling capacity at a low working fluid flow rate.

Considering the case of natural convection ($h = 5$ W/m^{2}K) and the channel shell liquid cooling, in the case with Re = 1,000, the maximum temperature on the coil winding drops to 142.9°C (416.0 K). Compared with the case of Re = 500, the temperature drops by 18.2 per

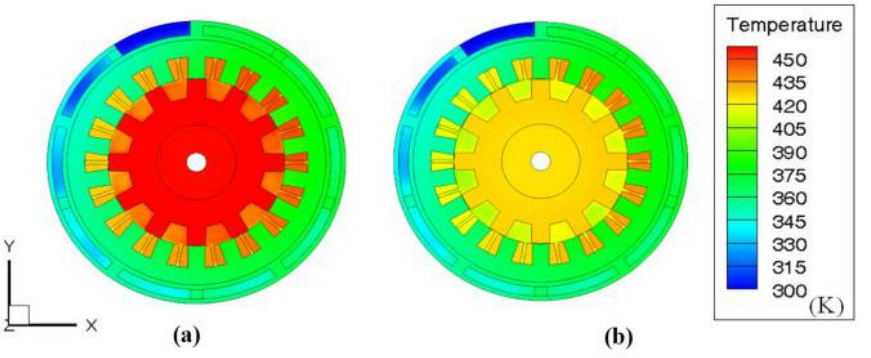

Figure 11.
Temperature distribution contours of liquid-cooled cooling system when the working flow rate Re = 500, $h = 5$W/m^{2}K and motor speed of 4,000 rpm

Notes: (a) channel shell; (b) extended channel shell

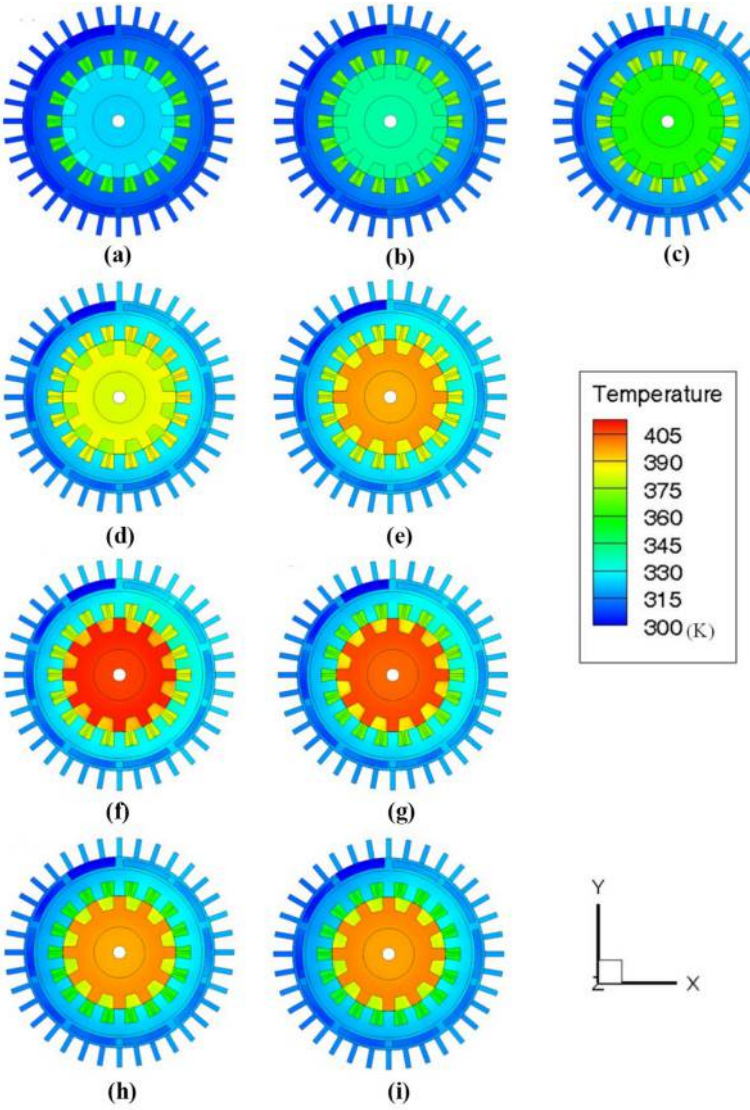

Notes: (a) 1,000 rpm; (b) 2,000 rpm; (c) 3,000 rpm; (d) 4,000 rpm; (e) 5,000 rpm; (f) 6,000 rpm; (g) 7,000rpm; (h) 8,000rpm; (i) 9,000rpm

Figure 12. Temperature distribution contours in motor components cooled using the liquid coolant and mounted fan for various motor speeds and Re = 1500

cent. The rise of the working fluid flow rate to Re = 1,500 results in the maximum coil winding temperature of 129.9°C (402.8 K), which is 9 per cent lower than that of Re = 1,000. When the coolant flow rate increases to Re = 2,000, the maximum coil winding temperature is only 124.3°C (397.4 K), which is 4.3 per cent lower than that of Re = 1,500. Although the increase of the flow rate increases the temperature drop, the rate of this temperature drop

shows a decreasing trend. As indicated by the classification of standard insulation material, the insulation material grade B with the maximum allowable temperature 130°C can be used for the case of Re = 2,000, which corresponds to the coil temperature of 124.3°C. The results indicate that the liquid-cooled heat cooling system enhances the heat dissipation effect and the increase of the flow rate also increases this enhancement. However, increasing the fluid flow rate increases the pump power consumption. Therefore, using an optimized heat sink may further enhance the cooling capacity of SRM under low flow rates to reduce the pump power consumption.

The optimum size and number of fins in the air-cooled cooling design is installed on the liquid-cooled enclosure. When the motor speed is 4,000 rpm and the ambient convection heat transfer coefficient is set to 5 W/m^2K, the performance of the channel shell and extended channel shell models are compared for Res of 500, 1,000, 1500 and 2,000. The results show when the channel shell is equipped with heat sink fins, the highest temperature component is still the rotor. When the coolant Re = 500, the maximum temperature of the coil winding is 167.6°C while the maximum temperature of the motor without heat sink fins was 174.9°C. Thus, the presence of the heat sink results in the temperature drops by 4.2 per cent. When the working fluid flow rate increases to Re = 1,000, the maximum coil winding temperature is 137.9°C, which shows 17.7 per cent temperature drop compared with the case of Re = 500. When the working fluid Re = 2,000, the maximum temperature on the coil winding is 124.3°C. Comparison between this case and its similar case but without heat sink, shows only 0.56 per cent enhancement in temperature drop. However, it was observed that the presence of heat sink results in a 4.2 per cent temperature drop in Re = 500. It can be seen that at low flow rate, the heat transfer effect is more obvious when the heat exchange area with air is increased (mounting fins), but when the working fluid flow rate increases, the effect of adding heat sink fins is not significant.

In the case of extended channel shell and natural convection (h = 5 W/m^2K), it is found that the maximum temperature on the coil winding is 160.2°C at Re = 500. The maximum coil temperature in a similar case but without heat sink was 166.5°C. Thus, using the heat sink decreases the temperature by 3.8 per cent. When the working fluid Re = 1,000, the maximum temperature on the coil winding is 130.4°C, which is 18.6 per cent lower than the fluid Re of 500. When the coolant Re is increased to 1500, the maximum temperature on the coil winding is 120.7°C, which is 7.4 per cent lower than the Re of 1,000. These results indicate that the presence of the liquid cooling can effectively reduce the maximum temperature of the coil winding. The liquid channel guides the working fluid to the extended channels of the shell in the front and rear covers. It can effectively reduce the temperature of the rotor inside the motor. The best cooling capacity of the liquid-cooled type in this study is the extended channel shell flow path with the fins mounted on the casing surface. When the working fluid Re = 2,000, the maximum temperature of the coil winding is 113.1°C; this is the best liquid cooling system so far. However, in this design, the working fluid operates at high flow rate, which consumes more energy in the circulating cooling water pump.

Now, the optimum heat sink fin design (36 fins of 30 mm height and 8 mm width) and a fan cooling for the air-cooled system and the best flow channel design (extended channel shell) are used. The model structure was depicted in Figure 4(b). Because of the presence of the fan, there is a stable airflow over the surface of the casing which generates forced convection. Table IV shows the maximum temperature of the coil winding for the best cooling design and various flow rates of Re = 500-2,000 at various motor speeds. Table IV shows that at the motor speed of 4,000, which is corresponding to the maximum coil loss, the maximum coil winding temperature is 143.2°C. However, in the same case but without the fan (the pure liquid cooled system) this temperature was 160.2°C. Hence, by using the fan,

the maximum temperature on the coil winding is decreased by 10.6 per cent, so that the forced convection has improved the cooling capacity. In accordance with the classification of the national standard insulation material, the insulation material grade F can be used.

When the working fluid flow rate is increased to Re = 1,000, it can be seen from Table IV that at the rotational speed is 4,000 rpm, the maximum temperature on the coil winding is 123.6°C, while in the case of natural convection (h = 5 W/m^{2}K), the maximum temperature of the coil winding was 130.4°C. Hence, using the fan results in temperature drops by 5.2 per cent. The case of natural convection cooling requires B grade insulation while by the presence of the fan, the required insulation grade is E. Increasing the flow rate to Re = 1500 and at the speed 4,000 rpm, the maximum coil winding temperature is 117.2°C while the similar case and without fan produces the maximum temperature of 120.7°C. Hence, in this case, using the fan results in 3.5°C (2.9 per cent) temperature drop. The insulation grade E is adequate for this temperature. The trend of the results shows when the flow rate of the working fluid is continuously increased, the influence of the airflow of the motor casing on the cooling capability is gradually reduced.

When the working fluid flow rate increases to Re = 2,000, the maximum temperature on the coil winding is 111.4°C, which in the same case the natural convection heat transfer provides 113.1°C. The temperature difference is only 1.7°C (1.5 per cent). According to the classification of national standard insulation materials, the insulation material grade E can be used the same as the working fluid flow Re of 1,500.

It can be concluded that in the case of the air-cooled and liquid-cooled hybrid cooling system, when the working fluid flow rate is low, the forced convection is significant for the improvement of the cooling performance. However, as the working fluid flow rate increases, the effect of the forced convection on the surface of the casing diminish. When the fluid flow rate is 1,500 and 2,000, the maximum temperature on the coil winding is 117.2°C and 111.4°C., respectively. Regarding the classification of insulating material, the grades of insulating materials for both cases is E. It is worth noticing that the high flow rate of 2,000 requires higher power for the fluid circulation using the water pump. Therefore, the optimum air-cooling and liquid-cooling hybrid design is Re = 1,500. Considering, the optimum air-cooling and liquid-cooling hybrid design, Figure 12 shows the temperature distribution in the motor components for various motor speeds when Re = 1,500. This figure shows almost a uniform temperature distribution in rotor, stator and coil windings.

5. Conclusion

A high power SRM is modeled from both aspects of the electromagnetic field analysis and the thermal analysis. The air-cooled cooling system using natural convection, the liquid-cooled cooling system and the air-cooled and liquid-cooled hybrid cooling systems were designed and analyzed for the SRM. Different combinations of the cooling approaches were also studied. The outcomes can be summarized as follows:

(1) The peak of copper loss occurs at a speed of 4,000 rpm. The increase of the motor speed increases the commutation frequency, thus, the excitation time of each motor winding shortened. As the results, the copper loss in the coil winding is gradually reduced.

(2) At low speed, the highest temperature component of the motor is the coil winding due to the copper loss. As the rotational speed of the motor increases, the iron loss increases. Thus, at high speed, the results show that the rotor is the hottest component of the motor due to the large iron loss and weak convection with internal air in the motor.

(3) A combination of the optimum heat sink and fan-cooled system is thermally analyzed. The maximum coil winding temperature is found to be 197.9°C when the motor speed is 4,000 rpm. It can be concluded that the air-cooled cooling system cannot ensure the motor always operates safely.

(4) The liquid-cooled cooling system can effectively reduce the temperature of the motor coil winding to be in the range of available standard insulations.

(5) Considering the best heat sink fin size and using the extended channel shell liquid-cooled cooling system (Re = 2,000) with air-cooled fan, the presence of the fins or their absence only changes the coil windings temperature by 0.56 per cent. Therefore, in the case of strong liquid flow rate the increase of heat transfer area does not induce a significant effect on the heat transfer rate.

(6) The best liquid-cooling system with the extended channel shell and optimized fins on the outer surface of the casing subject to natural convection (h = 5 W/m^{2}K) provides the maximum coil winding temperature of 113.1°C. Hence, by using the liquid-cooled cooling system under the natural convection, the insulation material grade E is adequate.

(7) The air-cooled and liquid-cooled hybrid cooling system with a working fluid flow rate of Re = 1,500 and in the presence of the mounted optimized fins can be selected as the best design cooling system for SRM.

References

Abbasian, M. and Jalali, H. (2017), "Thermal analysis of double stator switched reluctance machine (DSSRM) with and without a squirrel cage rotor", *Archives of Electrical Engineering*, Vol. 66 No. 1, pp. 189-198.

Ahmed, S. and Chamkha, A.J. (2014), "Hartmann Newtonian radiating MHD flow for a rotating vertical porous channel immersed in a Darcian porous regime: an exact solution", *International Journal of Numerical Methods for Heat and Fluid Flow*, Vol. 24 No. 7, pp. 1454-1470.

Al-Subaie, M. and Chamkha, A.J. (2003), "Steady natural convection flow of a particulate suspension through a Parallel-Plate channel", *Heat and Mass Transfer*, Vol. 39 No. 4, pp. 337-343.

Amorós, J.G., Andrada, P., Blanque, B. and Marin-Genesca, M. (2018), "Influence of design parameters in the optimization of linear switched reluctance motor under thermal constraints", *IEEE Transactions on Industrial Electronics*, Vol. 65 No. 2, pp. 1875-1883.

Bejan, A. (2013), *Convection Heat Transfer*, John Wiley and Sons, New York, NY.

Bostanci, E., Moallem, M., Parsapour, A. and Fahimi, B. (2017), "Opportunities and challenges of switched reluctance motor drives for electric propulsion: a comparative study", *IEEE Transactions on Transportation Electrification*, Vol. 3 No. 1, pp. 58-75.

Cabezuelo, D., Andreu, J., Kortabarria, I., Ibarra, E. and de Alegria, I.M. (2018), "Power modules for electric vehicles SRM converter", *PCIM Europe (2018); International Exhibition and Conference for Power Electronics, Intelligent Motion, Renewable Energy and Energy Management*, VDE.

Chamkha, A.J. (2002), "On laminar hydromagnetic mixed convection flow in a vertical channel with symmetric and asymmetric wall heating conditions", *International Journal of Heat and Mass Transfer*, Vol. 44, pp. 2509-2525.

Chamkha, A.J. (2003), "Effects of heat generation on g-Jitter induced natural convection flow in a channel with isothermal or isoflux walls", *Heat and Mass Transfer*, Vol. 39 No. 7, pp. 553-560.

Chamkha, A.J. and Al-Rashidi, S. (2010), "Analytical solutions for hydromagnetic natural convection flow of a particulate suspension through isoflux-isothermal channels in the presence of a heat source or sink", *Energy Conversion and Management*, Vol. 59, pp. 851-858.

Chamkha, A.J. and Al-Rashidi, S. (2013), "Solutions for MHD natural convection flow of a particulate suspension through a vertical channel with asymmetric thermal boundary conditions", *Heat Transfer Research*, Vol. 44 No. 2, pp. 215-243.

Chamkha, A.J., Grosan, T. and Pop, I. (2002), "Fully developed free convection of a micropolar fluid in a vertical channel", *International Communications in Heat and Mass Transfer*, Vol. 29 No. 8, pp. 1119-1127.

Chamkha, A.J., Grosan, T. and Pop, I. (2003), "Fully developed mixed convection of a micropolar fluid in a vertical channel", *International Journal of Fluid Mechanics Research*, Vol. 30 No. 3, pp. 251-263.

Chen, H. and Gu, J.J. (2013), "Switched reluctance motor drive with external rotor for fan in air conditioner", *IEEE/ASME Transactions on Mechatronics*, Vol. 18 No. 5, pp. 1448-1458.

Chiba, A. (2002), "Design of a switched reluctance drive and its application", *Journal-Magentics Society of Japan*, Vol. 26 No. 8, pp. 909-914.

Chinese National Standard (2018), Chinese National Standard, Classification of electrical insulation materials, CNS2147.

Chiu, H.C., Jang, J.H., Yan, W.M. and Shiao, R.B. (2017), "Thermal performance analysis of a 30 kW switched reluctance motor", *International Journal of Heat and Mass Transfer*, Vol. 114, pp. 145-154.

Diko, M., Rafajdus, P., Makys, P., Vavrus, V., Makarovic, J. and Saitz, J. (2017), Design and parameter analysis of short-flux path switched reluctance motor in electrical vehicles, *Environment and Electrical Engineering and 2017 IEEE Industrial and Commercial Power Systems Europe (EEEIC/I&CPS Europe), 2017 IEEE International Conference on*, *IEEE*, pp. 1-6.

Kiyota, K. and Chiba, A. (2012), "Design of switched reluctance motor competitive to 60-kW IPMSM in third-generation hybrid electric vehicle", *IEEE Transactions on Industry Applications*, Vol. 48 No. 6, pp. 2303-2309.

Krishnan, R. (2001), *Switched Reluctance Motor Drives: Modeling, Simulation, Analysis, Design, and Applications*, Chapts, CRC Press, New York, NY, pp. 1-4.

Kumar, J.P., Umavathi, J.C., Chamkha, A.J. and Pop, I. (2010), "Fully developed free convective flow of micropolar and viscous fluids in a vertical channel", *Applied Mathematical Modelling*, Vol. 35, pp. 1175-1186.

Li, S., Zhang, S., Habetler, T.G. and Harley, R.G. (2017), "A survey of electromagnetic-Thermal modeling and design optimization of switched reluctance machines", *Electric Machines and Drives Conference (IEMDC), IEEE International*, *IEEE*, pp. 1-7.

Mills, A.F. (1999), *Heat Transfer*, 2nd Ed., Prentice-Hall, New York, NY.

Moallem, M. and Ong, C.M. (1990), "Predicting the torque of a switched reluctance machine from it's finite element field solution", *IEEE Transactions on Energy Conversion*, Vol. 5 No. 4, pp. 733-739.

Nutan, S., Panda, A.K. and Panda, S. (2017), "Speed control with torque ripple reduction of switched reluctance motor by many optimizing liaison technique", *Journal of Electrical Systems and Information Technology*, Vol. 20 No. 3, pp. 909-921.

Ohyama, K., Nashed, M.N.F., Aso, K., Fujii, H. and Uehara, H. (2006), "Design using finite element analysis of a switched reluctance motor for electric vehicle", *Information and Communication Technologies, ICTTA '06, 2nd*, pp. 727-732.

Rahman, M., Oztop, H., Mekhilef, S., Saidur, R., Chamkha, A.J., Ahsan, A. and Al-Salem, K. (2014), "A finite element analysis on combined convection and conduction in a channel with a thick walled cavity", *International Journal of Numerical Methods for Heat and Fluid Flow*, Vol. 24 No. 8, pp. 1888-1904.

Ranjini, K.S.S. and Murugan, S. (2018), "Design and performance comparison of permanent magnet brushless motors and switched reluctance motors for extended temperature applications", *Progress in Electromagnetics Research M*, Vol. 67, pp. 137-146.

Sundaram, M., Navaneethan, P. and Vasanthakumar, M. (2009), Magnetic analysis and comparison of switched reluctance motors with different stator pole shapes using a 3D finite element method, *International Conference on Control, Automation, Communication and Energy Conservation*, *Perundurai, Tamilnadu*.

Umavathi, J.C., Chamkha, A.J. and Mohiuddin, S. (2016), "Combined effect of variable viscosity and thermal conductivity on free convection flow of a viscous fluid in a vertical channel", *International Journal of Numerical Methods for Heat and Fluid Flow*, Vol. 26 No. 1, pp. 18-39.

Umavathi, J.C., Chamkha, A.J., Mateen, A. and Kumar, J.P. (2008), "Unsteady magnetohydroynamic two fluid flow and heat transfer in a horizontal channel", *International Journal of Heat and Technology*, Vol. 26, pp. 121-133.

Yakhot, V. and Orszag, S.A. (1986), "Renormalization group analysis of turbulence I. Basic theory", *Journal of Scientific Computing*, Vol. 1 No. 1, pp. 3-51.

Yasa, Y., Sozer, Y. and Garip, M. (2018), "Loss analysis of high speed switched reluctance machine with integrated simulation methods", *International Journal of Applied Electromagnetics and Mechanics*, Vol. 56 No. 3, pp. 479-497.

Yu, Q., Wang, X. and Cheng, Y. (2017), "Electromagnetic and thermal coupled analysis of can effect of a novel canned switched reluctance machine as a hydraulic pump drive", *International Journal of Applied Electromagnetics and Mechanics*, Vol. 54 No. 1, pp. 131-140.

Zhe, H. Hui, G. and Guobiao, G. (2009), Review of liquid cooling technology for rotor of turbo generator and application research of open channel evaporative cooling technology, 2009 International Conference on Electrical Machines and Systems.

Corresponding author
Wei-Mon Yan can be contacted at: wmyan@ntut.edu.tw and Mohammad Ghalambaz can be contacted at: m.ghalambaz@gmail.com